


## Article

# Determination of Al-2.18Mg-1.92Li Alloy's Microstructure Degradation in Corrosive Environment

Franjo Kozina <sup>1,\*</sup>, Zdenka Zovko Brodarac <sup>1,\*</sup> , Sandra Brajčinović <sup>1</sup> and Mitja Petrič <sup>2</sup><sup>1</sup> Faculty of Metallurgy, University of Zagreb, 44000 Sisak, Croatia; smitic@simet.hr<sup>2</sup> Faculty of Natural Sciences and Engineering, University of Ljubljana, SI-1000 Ljubljana, Slovenia; mitja.petric@omm.ntf.uni-lj.si

\* Correspondence: fkozin@simet.hr (F.K.); zovko@simet.hr (Z.Z.B.); Tel.: +385-44-533-380 (F.K. &amp; Z.Z.B.)

**Abstract:** The utilization of aluminum-lithium-magnesium (Al-Li-Mg) alloys in the transportation industry is enabled by excellent engineering properties. The mechanical properties and corrosion resistance are influenced by the microstructure development comprehending the solidification of coherent strengthening precipitates, precipitation of coarse and angular equilibrium phases as well as the formation and widening of the Precipitate-free zone. The research was performed to determine the microstructure degradation of Al-2.18Mg-1.92Li alloy in a corrosive environment using electrochemical measurements. The solidification sequence of the Al-2.18Mg-1.92Li alloy, obtained using Thermo-Calc software support, indicated the transformation of the  $\alpha_{Al}$  dendritic network and precipitation of AlLi ( $\delta$ ),  $Al_2LiMg$  (T), and  $Al_8Mg_5$  ( $\beta$ ) phase. All of the phases are anodic with respect to the  $\alpha_{Al}$  enabling microstructure degradation. To achieve higher microstructure stability, the sample was solution hardened at 520 °C. However, the sample in as-cast condition showed a lower corrosion potential (−749.84 mV) and corrosion rate (17.01 mm/year) with respect to the solution-hardened sample (−752.52 mV, 51.24 mm/year). Higher microstructure degradation of the solution-hardened sample is a consequence of  $\delta$  phase precipitation at the grain boundaries and inside the grain of  $\alpha_{Al}$ , leading to intergranular corrosion and cavity formation. The  $\delta$  phase precipitates from the Li and Mg enriched the  $\alpha_{Al}$  solid solution at the solution-hardening temperature.

**Keywords:** Al-Mg-Li alloy; solidification sequence; as-cast; solution hardening; microstructure; degradation



**Citation:** Kozina, F.; Brodarac, Z.Z.; Brajčinović, S.; Petrič, M. Determination of Al-2.18Mg-1.92Li Alloy's Microstructure Degradation in Corrosive Environment. *Crystals* **2021**, *11*, 338. <https://doi.org/10.3390/cryst11040338>

Academic Editor: Hyokyung Sung

Received: 21 February 2021

Accepted: 25 March 2021

Published: 27 March 2021

**Publisher's Note:** MDPI stays neutral with regard to jurisdictional claims in published maps and institutional affiliations.



**Copyright:** © 2021 by the authors. Licensee MDPI, Basel, Switzerland. This article is an open access article distributed under the terms and conditions of the Creative Commons Attribution (CC BY) license (<https://creativecommons.org/licenses/by/4.0/>).

## 1. Introduction

The aluminum-lithium (Al-Li) alloys are characterized by density reduction, stiffness increase, increase in fracture toughness, and fatigue crack growth resistance [1]. The stability at elevated temperatures, a higher modulus of elasticity, and additional weight savings enable Al-Li alloys to substitute 2xxx and 7xxx series of Al alloys in the transportation industry. Compared to copper (Cu) and zinc (Zn), Li additions directly reduce density and increase the modulus of elasticity. Each 1 wt.% of Li added decreases density by 3% and increases the modulus of elasticity by 6% and stiffness by 5% for additions up to 4.2 wt.% Li [2]. The primary strengthening precipitate in Al-Li alloys is the metastable  $Al_3Li$  ( $\delta'$ ) phase [3]. Unlike intermetallic precipitates in 2XXX and 7XXX series of Al alloys, the  $\delta'$  phase stays spherical and coherent with the  $\alpha_{Al}$  matrix at high temperatures retaining the stability of microstructure and mechanical properties [4–7]. The preferred precipitation of the  $\delta'$  phase in Al-Li alloys can be achieved with Mg additions. By reducing the solid solubility of Li in  $\alpha_{Al}$  solid solution and partially substituting Li in the  $\delta'$  phase lattice, Mg additions increase the volume fraction of the  $\delta'$  phase [8]. Based on chemical composition, thermodynamic parameters, and processing parameters, the microstructure development [9] of Al-Li-Mg alloys also comprehends the solidification of coherent precipitates that alter the planar slip band formation, precipitation of coarse and angular equilibrium phases as well as the formation and widening of Precipitate-free

zone (PFZ) [10,11]. The microstructure development during solidification or processing directly influences mechanical properties [12] and corrosion behavior of Al-Li-Mg alloys. The microstructure degradation in corrosive environments will affect the applicability of Al-Li-Mg alloys in the transportation industry [13].

Despite the high reactivity of Li, Al-Li-Mg alloys exhibit good resistance to uniform microstructure degradation originating from surface passive film formation [14]. However, they are strongly susceptible to cavity formation, intergranular degradation, and exfoliation depending on the composition of the environment and microstructure development [15]. The cavity formation occurs when the Al-Li-Mg alloys are exposed to environments outside 3 pH–10 pH [16], and it can act as a precursor to the other microstructure degradation processes [17].

The intergranular degradation selectively attacks the grain boundaries and adjacent matrix without affecting the grains. The progress of microstructure degradation in Al-Li-Mg alloys is described by the Anodic dissolution theory and PFZ breakdown model [18].

Anodic dissolution of the grain-boundary precipitates results in continuous anodic path formation along the grain boundaries leading to the dissolution of the  $\alpha_{Al}$  matrix and intergranular degradation [19]. In Al-Li-Mg alloys, the metastable  $Al_3Li$  ( $\delta'$ ) [20], stable  $AlLi$  ( $\delta$ ), ternary  $Al_2LiMg$  (T), and secondary eutectic  $Al_8Mg_5$  ( $\beta$ ) phases are anodic with respect to the  $\alpha_{Al}$  matrix contributing to the microstructure degradation in corrosive environments [21]. The metastable  $\delta'$  is the most important hardening precipitate that solidifies homogeneously distributed in the  $\alpha_{Al}$  matrix. The similarities in the structure and lattice parameters between the  $\alpha_{Al}$  matrix and the  $\delta'$  phase manifest with low-coherency strain and low-interfacial energy leading to the order hardening [22]. The detrimental effect of the  $\delta'$  phase on intergranular degradation is caused by interaction with dislocations leading to the microstructure texture development. The stable  $\delta$  phase precipitates inside the grains of the  $\alpha_{Al}$  matrix on the previously precipitated  $\delta'$  phase. The coarsening of the  $\delta$  phase that occurs during the aging process increases the degradation rate [17]. The solidification of the T phase has less effect on the microstructure degradation of the alloy due to its nucleation at the high-angle grain boundaries and the grain boundary triple points [23,24]. The initial nucleation at the grain boundaries limits the negative impact of the  $\beta$  phase on the Al-Li-Mg alloy microstructure degradation [25].

The PFZ breakdown model correlates the effect of chloride ( $Cl^-$ ) or halide ions on the PFZ with cavity formation and exfoliation in heat-treated Al alloys. Since the electrochemical potential of the PFZ is lower compared to the potential of enriched  $\alpha_{Al}$  matrix and grain-boundary precipitates, a localized attack will result in microstructure degradation [24]. The formation of PZF in Al-Li-Mg alloys depends on the Li/Mg ratio. When the Li/Mg ratio is high, the peritectic reaction between liquid (L) and  $\delta'$  leads to the precipitation of the stable  $\delta$  phase. The stable  $\delta$  phase precipitates inside the grains of the  $\alpha_{Al}$  matrix. The formation of PFZ in the alloys containing 2 wt.% > Mg and a lower Li/Mg ratio comprehends precipitation of the T phase at the expense of the previously precipitated  $\delta'$  and the bulked  $\alpha_{Al}$  matrix [26,27].

The exfoliation is characterized by lamellar surface attack of the alloy containing a highly directional grain structure. It is an intergranular degradation based on the galvanic interaction between grain-boundary precipitates and the adjacent matrix. During the exfoliation process, the Al from the  $\alpha_{Al}$  matrix and precipitates is transformed into the non-soluble highly voluminous hydrated aluminum oxide ( $Al(OH)_3$ ), which causes wedging and enables further attack. The wedging effect of the degradation products can lead to cavity progression, flaking, powdering, blistering or SCC. The texture originates from the interaction between dislocations and the  $\delta'$  phase. Additionally, high oxidation and hydrogen release during the dissolution of the  $\beta$  phase are the main causes of Al-Li-Mg alloys' exfoliation appearance [28].

The goal of the research is to determine the microstructure degradation of Al-2.18Mg-1.92Li alloys in as-cast and solution-hardened conditions during electrochemical testing. The solution hardening was performed to dissolve all precipitated phases and enrich the  $\alpha_{Al}$

matrix. By dissolving the anodic phases, higher resistance to microstructure degradation is expected. The application of electrochemical measurements, mainly Time dependence of open-circuit potential and Tafel polarization curves, enabled the assessment of sample stability, corrosion potential, and corrosion rate. The progress of the accelerated degradation process and its impact on the macrostructure and microstructure will be estimated visually using light microscopy. The applied method is used to simulate the material degradation in various types of outdoor services, especially in marine and automotive applications.

## 2. Materials and Methods

To synthesize the alloy, an Al block of technical purity (99.0%) was placed into a graphite crucible coated with boron nitride (BN) and deposited into an induction melting furnace. The alloy synthesis was performed in the new (never used) graphite crucible containing a sufficient amount of carbon necessary to achieve and retain the melting temperature of the raw materials. The graphite crucible was coated to prevent impurity pickup from refractory materials. The controlled atmosphere was obtained through the argon (Ar) introduction. Maintaining a controlled atmosphere during melting and full shielding of the melt was ensured by the crucible cover. To avoid the pickup of impurities originating from raw materials, the alloying was performed using an Mg rod of 99.98% purity and a Li rod of 99.8% purity. The Mg and Li were wrapped into an Al foil (commercial purity) and placed into a steel bell coated with BN. The alloying was performed at 720 °C by introducing a previously prepared steel bell into molten Al. The homogeneous distribution of alloying elements was ensured through reheating to 740 °C and stirring the melt using the steel bell coated with boron nitrite. Casting was performed into a permanent steel mold at 740 °C without a protective atmosphere of Ar. The geometry of the sample with indicated sampling for corrosion testing is given in Figure 1.

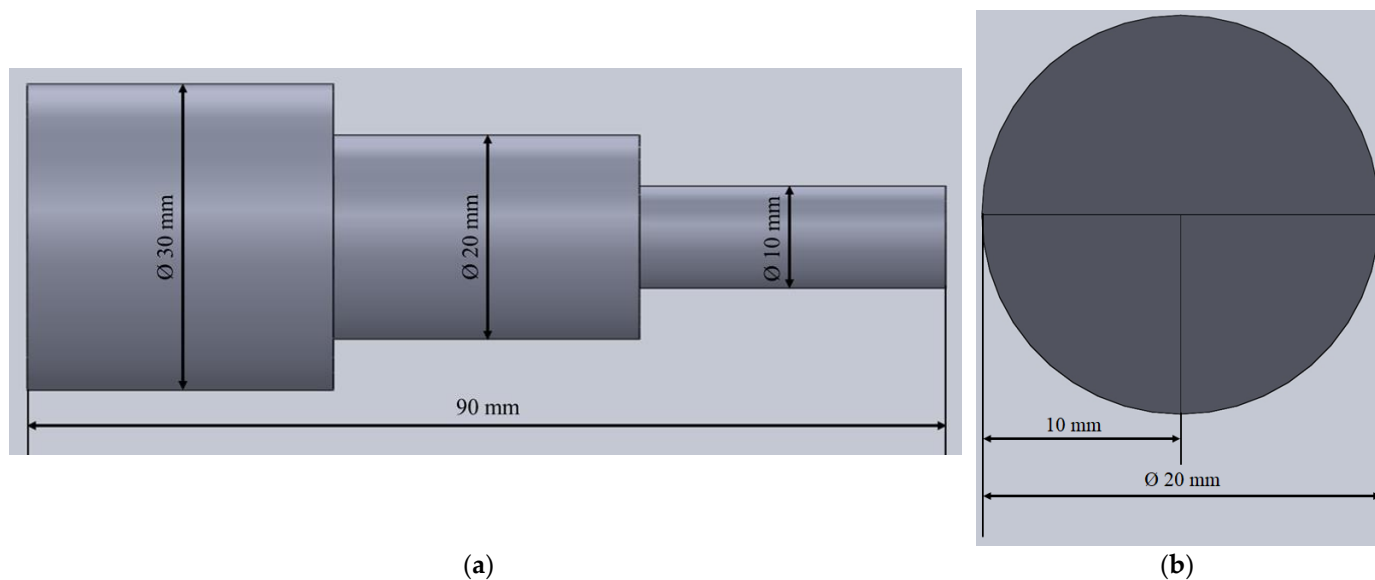


**Figure 1.** The cast sample geometry with: (a) Indicated dimensions; (b) Indicated sampling for corrosion testing.

The sample is 90 mm in length comprising of three cylinders with different diameters. The largest cylinder is 30 mm in diameter, while the smallest cylinder has a diameter of 10 mm (Figure 1a).

The produced alloy's chemical composition was determined using inductively coupled plasma with mass spectroscopy (ICP-MS) on the Agilent Technologies Inductively coupled plasma-mass spectrometer. Before initiating measurements, the spectrometer was calibrated using standardized calibrating solutions. Due to the high reactivity of Li, the ICP-MS was additionally calibrated using solutions containing 1, 10, 50, 100 mg/m<sup>3</sup> of Li.

Based on the chemical composition results, the Thermo–Calc software support was used to calculate the equilibrium and non-equilibrium solidification sequence and reactions in liquid and solid states. The solidification sequence was calculated using the TCAL6 v6.0 technical sheet for Al. The prediction of non-equilibrium solidification was based on the classic Scheil–Gulliver model.

The obtained solidification sequence and corresponding temperatures were used to select the solution-hardening temperature. The sample was solution hardened at 520 °C for 4 h and quenched in water.

The electrochemical measurements were performed using a standard three-electrode cell with a saturated calomel reference electrode (SEC), a platinum counter electrode, and a 1 cm<sup>3</sup> exposed surface of a working electrode sample. The solution for the electrochemical testing was obtained by dissolving 234 g of sodium chloride (NaCl) and 50 g of potassium nitrate (KNO<sub>3</sub>) in water. Afterwards, 6.3 mL of HNO<sub>3</sub> was added and the solution was diluted to 1 L by adding distilled water. The obtained solution had a pH of 0.4. To avoid the influence of degradation products on the bulk-solution chemistry, approximately 250 mL of solution was used for each test. The samples for corrosion testing were taken from the middle cylinder of the cast sample with a diameter of Ø 20 mm and a length of 30 mm. The middle cylinder was cut into quarters (Figure 1b). One quarter was used to estimate microstructure degradation in as-cast condition, while the other quarter was solution hardened first and then subjected to corrosion testing. The electrochemical measurements were performed using potentiostat/galvanostat Parstat 2273 at room temperature (19 ± 2 °C) with a 0.5 mV/s scan rate. Before initiating the corrosion measurements, the Open circuit potential ( $E_{\text{opc}}$ ) was stabilized for 600 s. The Tafel extrapolation method was performed using potentiodynamic polarization in the potential range from –250 mV to +250 mV vs  $E_{\text{corr}}$  with a scan rate of 0.5 mV/s. The corrosion potential ( $E_{\text{corr}}$ ), corrosion current density ( $i_{\text{c}}$ ), anode slope ( $B_{\text{a}}$ ), cathode slope ( $B_{\text{c}}$ ), and corrosion rate ( $v_{\text{corr}}$ ) were extrapolated from Tafel's polarization curves using PowerCorr™ software support.

The metallographic analysis was performed on the samples in as-cast and solution-hardened conditions before and after electrochemical testing. The samples were prepared using standard grinding and polishing techniques. The samples for macrostructural analysis were etched using Poulton's etching solution (60 mL of hydrochloric acid (HCl), 30 mL of nitric acid (HNO<sub>3</sub>), 5 mL of hydrofluoric acid (HF), and 5 mL water (H<sub>2</sub>O)) and observed on the stereo microscope Olympus SZ11. The samples for microstructural analysis were etched using Weck's (4 g KMnO<sub>4</sub>, 1 g NaOH, and 100 mL H<sub>2</sub>O) and Keller's (1 volume part of HF, 1.5 volume part of HCl, 2.5 volume parts of HNO<sub>3</sub>, and 95 volume parts of water). The microstructure was analyzed on an Olympus GX51 inverted metallographic microscope equipped with Olympus Stream Motion 2.4.3. software support. The metallographic analysis of the tested samples was performed on the exposed surface and cross-section perpendicular to the exposed surface. The cross-section of the samples was analyzed in polished and etched conditions after standard metallographic preparation. The scanning electron microscope (SEM) Tescan Vega TS 5136 MM equipped with an energy-dispersive spectrometer was used to quantify the amounts of Al and Mg in as-cast and solution-hardened samples. Since EDS cannot determine light elements, such as Li, the X-Ray Diffraction (XRD) was used to identify Li-containing intermetallic phases in the as-cast sample. The XRD was performed on a PANalytical X'Pert PRO diffractometer with non-monochromated X-rays produced by an Empyrean Cu anode tube operating at 45 kV and 40 mA. The calibration was not performed because the standards are used for powder samples.

### 3. Results

The results of the chemical analysis are given in Table 1.

The produced alloy contains 2.18 wt.% of Mg and 1.92 wt.% of Li (Table 1). The Mg content of 2.18 wt.% and lower Li/Mg ratio (Li/Mg = 0.88) indicates preferred solidification of T phase.

The solidification sequence of Al-2.18Mg-1.92Li alloy under equilibrium conditions is shown in Figure 2a,b, while the following invariant reactions and corresponding temperatures are given in Table 2.

**Table 1.** The results of the chemical analysis.

Element	Amount, wt. %
Li	1.92
Mg	2.18
Al	balance

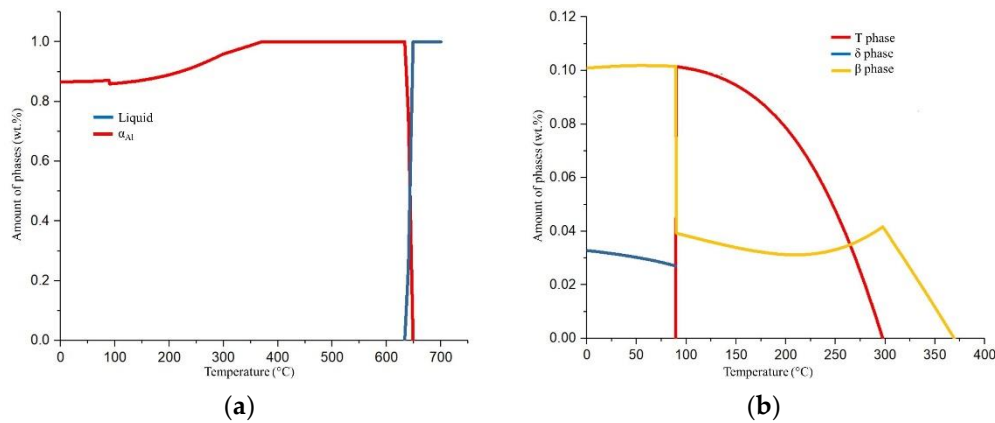


**Figure 2.** The equilibrium solidification sequence of the Al-2.18Mg-1.92Li alloy: (a) transformation of the  $\alpha_{Al}$  dendritic network and (b) solid-state diffusion processes in the  $\alpha_{Al}$  dendritic network. Abbreviations: the stable AlLi ( $\delta$ ), ternary  $Al_2LiMg$  (T), and secondary eutectic  $Al_8Mg_5$  ( $\beta$ ) phases.

**Table 2.** The invariant reactions and corresponding temperatures for the Al-2.18Mg-1.92Li alloy equilibrium solidification sequence. Abbreviations: the stable AlLi ( $\delta$ ), ternary  $Al_2LiMg$  (T), secondary eutectic  $Al_8Mg_5$  ( $\beta$ ) phases, and liquid (L).

Reaction	Temperature, °C	Composition, wt. %		
		Al	Mg	Li
$L \rightarrow \alpha_{Al}$	640	96.59	1.66	1.75
$\alpha_{Al} \rightarrow \delta + \alpha_{Al}'$	360	78.44	4.77	16.79
$\alpha_{Al} + \delta \rightarrow T + \alpha_{Al}''$	290	71.53	17.02	11.46
$\alpha_{Al}'' \rightarrow \beta + \delta + \alpha_{Al}'''$	89.15	49.95	44.73	5.31

The equilibrium solidification sequence begins with the transformation of the  $\alpha_{Al}$  dendritic network at 640 °C (Figure 2a) containing 96.59 wt.% Al, 1.66 wt.% Mg, and 1.75 wt.% Li (Table 2). The rest of the equilibrium solidification sequence is based on the solid-state diffusion processes in the  $\alpha_{Al}$  dendritic network (Figure 2b). The stable  $\delta$  phase precipitates at 360 °C containing 78.44 wt.% Al, 4.77 wt.% Mg, and 16.79 wt.% Li (Table 2). The amount of precipitated  $\delta$  phase grows until 290 °C when the T phase begins to precipitate (Figure 2b) containing 71.53 wt.% Al, 17.02 wt.% Mg, and 11.46 wt.% Li (Table 2). The solidification sequence ends with the precipitation of the  $\beta$  phase containing 49.95 wt.% Al, 44.73 wt.% Mg, and 5.31 wt.% Li at 89.15 °C (Table 2). The precipitation of the  $\beta$  phase suppresses the T phase's precipitation and increases the precipitation of the  $\delta$  phase (Figure 2b) and the  $\alpha_{Al}$  dendritic network (Figure 2a).

The non-equilibrium solidification sequence of Al-2.18Mg-1.92Li alloy is shown in Figure 3, while the following invariant reactions and corresponding temperatures are given in Table 3.

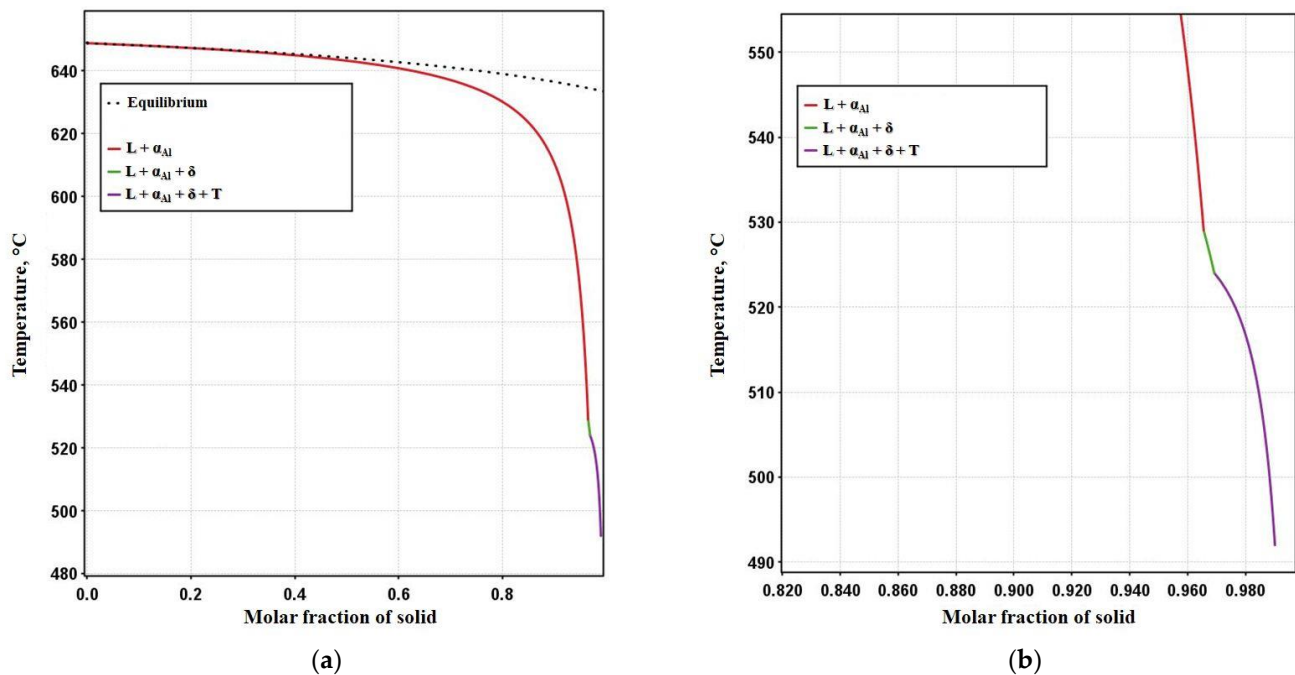


**Figure 3.** The non-equilibrium solidification sequence of Al-2.18Mg-1.92Li alloy based on the classic Scheil–Gulliver model: (a) the curve covering complete solidification and (b) the segment of the curve emphasizing the phase solidification.

**Table 3.** The invariant reactions and corresponding temperatures for the Al-2.18Mg-1.92Li alloy’s non-equilibrium solidification sequence.

Reaction	Temperature, °C
$L \rightarrow \alpha_{Al}$	649
$L \rightarrow \delta + \alpha_{Al}$	529
$L \rightarrow T + \delta + \alpha_{Al}$	524

The non-equilibrium solidification exclusively comprehends transformations and solidification in L state. The solidification sequence begins with the transformation of the  $\alpha_{Al}$  dendritic network at 649 °C (Figure 3 and Table 3) followed by the solidification of the  $\delta$  phase at 529 °C and T phase at 524 °C (Figure 3 and Table 3). The solidification of the secondary eutectic  $\beta$  phase is not recognized by this model. The alloy exhibits a wide solidification range indicating a greater temperature gradient and degree of undercooling (Figure 3, Equilibrium solidification line). The solidification with a higher degree of undercooling enables microstructure refinement, improvement in alloy properties, and microstructure degradation resistance.

The macrostructure of the sample in as-cast and solution-hardened conditions is given in Figure 4.

The macrostructure of the sample in as-cast condition has a heterogeneous grain morphology consisting of chill, columnar, and equiaxed zones. The narrow chill zone formed at the surface of the sample is followed by the zone of columnar grains. The zone of equiaxed grains is in the center of the sample (Figure 4a). The solution hardening led to homogenization in the grain morphology (Figure 4b).

The results of XRD analysis are given in Figure 5.

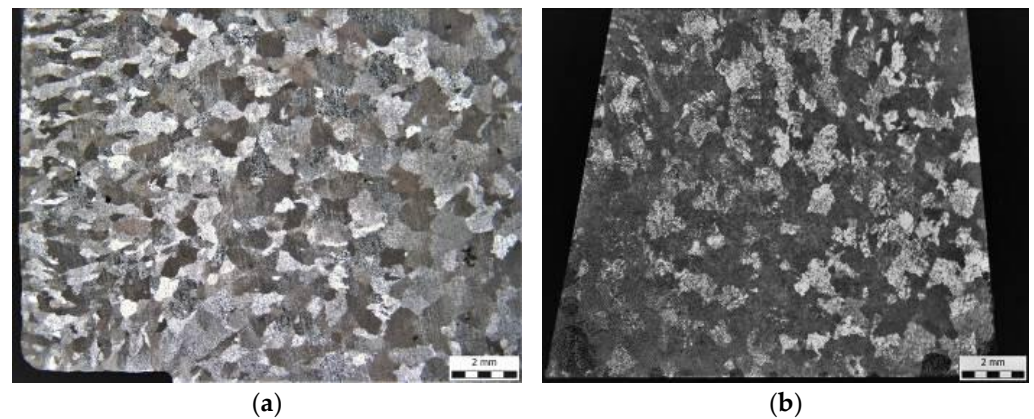


**Figure 4.** The macrostructure of the sample in: (a) as-cast condition and (b) solution-hardened condition.

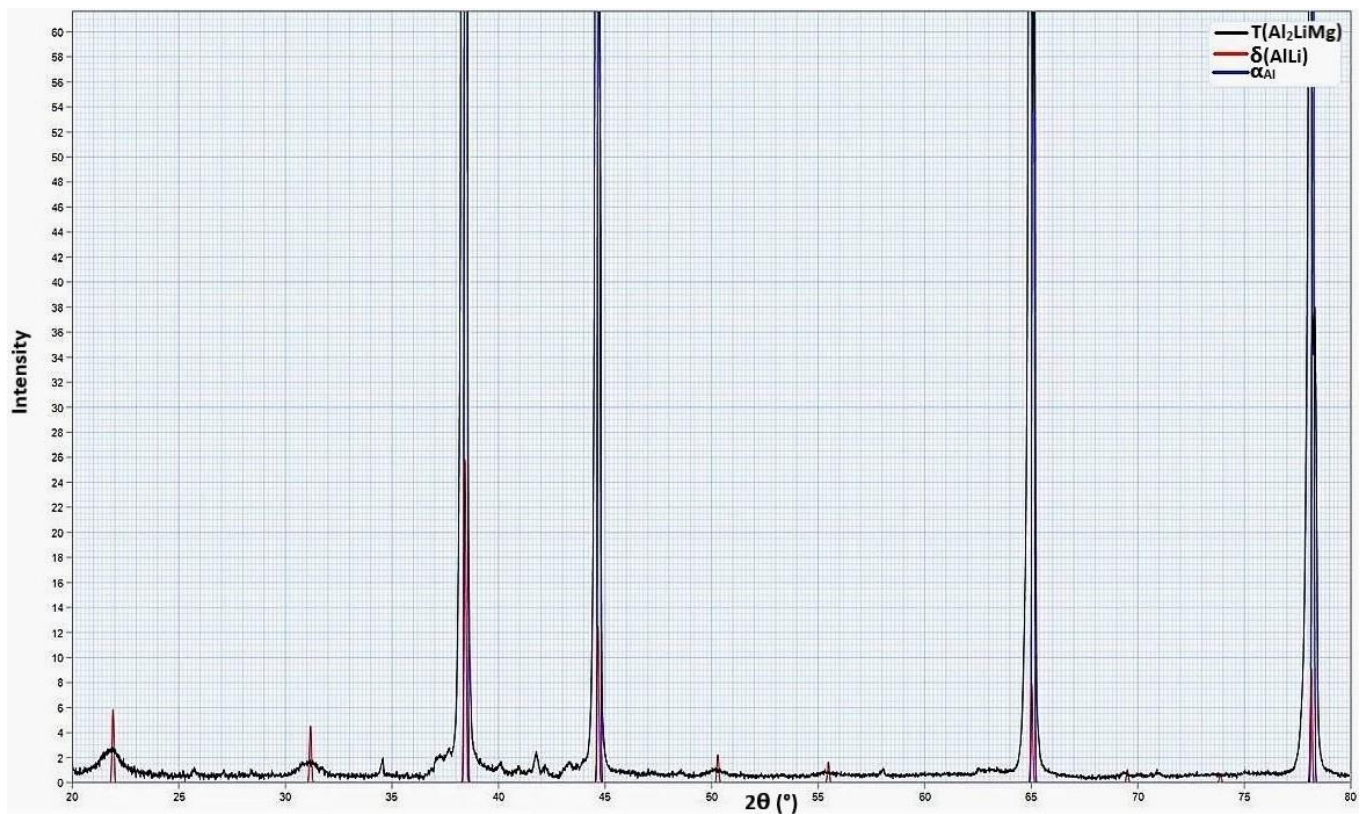


**Figure 5.** The X-Ray Diffraction (XRD) diffractogram of the sample in as-cast condition.

The XRD of the sample in the as-cast condition identified the presence of the  $\alpha_{Al}$  matrix and the T and  $\delta$  phases (Figure 5).

The microstructure of the sample in the as-cast condition is given in Figure 6a,b. Figure 6c represents the Scanning Electron Image (SEI) with the indicated details for EDS analysis. The results of the EDS analysis are given in Table 4.

The microstructure of the sample in the as-cast condition consists of the  $\alpha_{Al}$  dendritic network (Figure 6a) and precipitates located between the branches of  $\alpha_{Al}$  dendrites (Figure 6a). The precipitates located between differently oriented  $\alpha_{Al}$  dendrites have coarse morphology corresponding to the secondary eutectic  $\beta$  phase (Figure 6b). The precipitates located between the secondary branches of  $\alpha_{Al}$  dendrites have finer morphology and can be identified as T phase (Figure 6b). The  $\alpha_{Al}$  dendrites consist of 98.08 wt.% Al and 1.92 wt.%

Mg (Figure 6, Table 4, detail 1). The reduced solid solubility of Mg in  $\alpha_{Al}$  matrix with respect to temperature resulted in Mg segregation to interdendritic areas (Figure 6, Table 4, detail 2). Consequently, the Mg content in interdendritic areas increased to 3.37 wt.% Mg. The highest Mg content of 4.49 wt.% is connected to the secondary eutectic  $\beta$  phase (Figure 6, Table 4, detail 3).

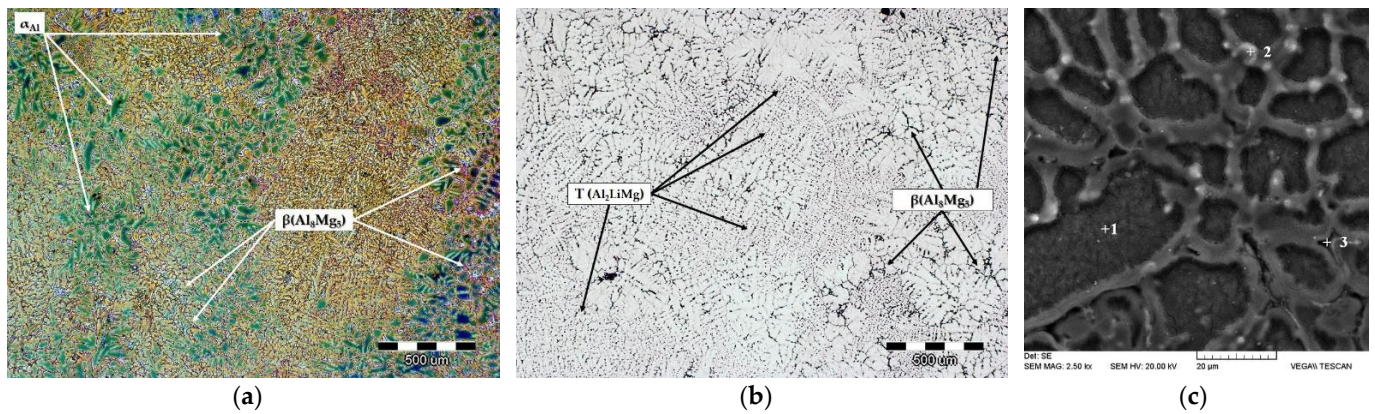


**Figure 6.** The microstructure of the sample in as-cast condition: (a) etched with Weck's etching solution; (b) etched with Keller's etching solution; (c) SEI with indicated details for EDS analysis.

**Table 4.** The results of the EDS analysis of the as-cast sample performed on the details indicated in Figure 6c.

Detail	Al, wt.%	Mg, wt.%
1	98.08	1.92
2	96.22	3.78
3	95.51	4.49

The microstructure of the solution-hardened sample is given in Figure 7a,b. Figure 7c represents the SEI with the indicated details for EDS analysis given in Table 5.

The microstructural analysis of the solution-hardened sample reveals the  $\alpha_{Al}$  grains (Figure 7) and residual phase precipitated inside the grains of  $\alpha_{Al}$  (Figure 7) corresponding to the  $\delta$  phase (Figure 7). The T phase and  $\beta$  phase were not detected in the solution-hardened sample. The  $\delta$  phase is homogeneously distributed inside the grains of the  $\alpha_{Al}$  matrix with no PFZ near the grain boundaries (Figure 7a,b). The solution hardening resulted in equal distribution of Mg inside the grains (3.29 wt.% Mg) and on the grain boundaries (3.44 wt.% Mg) (Table 5, details 1 and 2). The lowest amount of Mg (2.79 wt.% Mg) was measured in the  $\delta$  phase (Table 5, detail 3).

The results of electrochemical testing are given in Figure 8.

**Table 5.** The results of the EDS analysis of the solution-hardened sample performed on the details indicated in Figure 7c.

Detail	Al, wt.%	Mg, wt.%
1	96.71	3.29
2	96.56	3.44
3	97.21	2.79



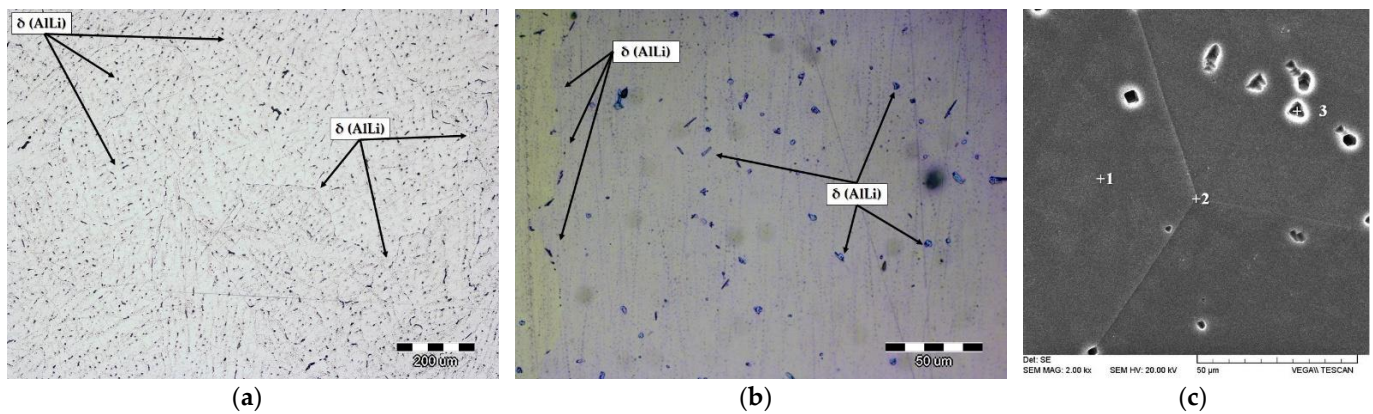


**Figure 7.** The microstructure of the sample in solution-hardened condition: (a) etched with Keller's etching solution; (b) etched with Weck's etching solution; (c) SEI with indicated details for EDS analysis.

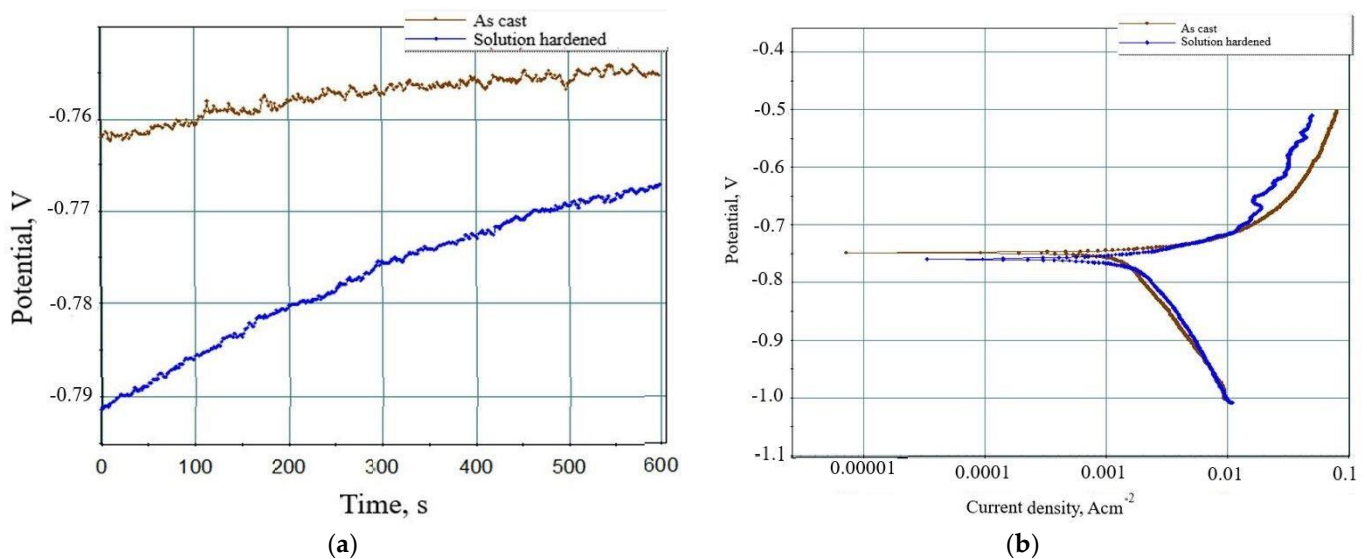


**Figure 8.** The results of electrochemical testing: (a) Time dependence of open circuit potential ( $E_{opc}$ ); (b) Tafel polarization curves.

The results of the electrochemical testing are given in are given in Table 6.

**Table 6.** The invariant reactions and corresponding temperatures for the Al-2.18Mg-1.92Li alloy equilibrium solidification sequence. Abbreviations: the corrosion potential ( $E_{corr}$ ), corrosion current density ( $i_c$ ), anode slope ( $B_a$ ), cathode slope ( $B_c$ ), and corrosion rate ( $v_{corr}$ ).

Sample	$E_{corr}$ (mV)	$i_{corr}$ ( $\mu A \cdot cm^2$ )	$B_a$ (mV/dec)	$B_c$ (mV/dec)	$V_{corr}$ (mm/Year)
As-cast	-749.84	$1.52 \cdot 10^3$	38.60	296.26	17.01
Solution-hardened	-752.52	$4.61 \cdot 10^3$	174.76	742.96	51.24

The negative corrosion potential ( $E_{corr}$ ) recorded during Time dependence of open circuit potential measurements indicates instability of samples and their dissolution during testing (Figure 8a and Table 6). The sample in as-cast condition shows less negative potential (-755 mV) compared to the solution-hardened sample (-767 mV), indicating higher resistance to microstructure degradation (Table 6). However, an increase in the corrosion potential of the solution-hardened sample during the Time dependence of open circuit potential measurements points to spontaneous passivation (Figure 8a). The Tafel polarization curves ratify the higher stability of the sample in as-cast condition compared to the solution-hardened sample (Figure 8b). The extrapolation of obtained Tafel polarization

curves indicates more negative corrosion potential ( $-752.52$  mV), higher current density ( $4.61 \cdot 10^3 \mu\text{A}\cdot\text{cm}^2$ ), anode slope ( $174.76$  mV/dec), cathode slope ( $742.96$  mV/dec), and corrosion rate ( $51.24$  mm/year) for the solution hardened sample. The higher current density and anode slope are consequences of the dealloying and dissolution of Al (Table 6). The higher cathode slope is attributed to the solution reduction and local increase in pH value. The local increase in the pH value of the testing solution led to the spontaneous passivation of the solution-hardened sample and an increase in corrosion potential (Figure 8a and Table 6).

The macrostructure and microstructure of the samples after electrochemical testing are given in Figure 9.

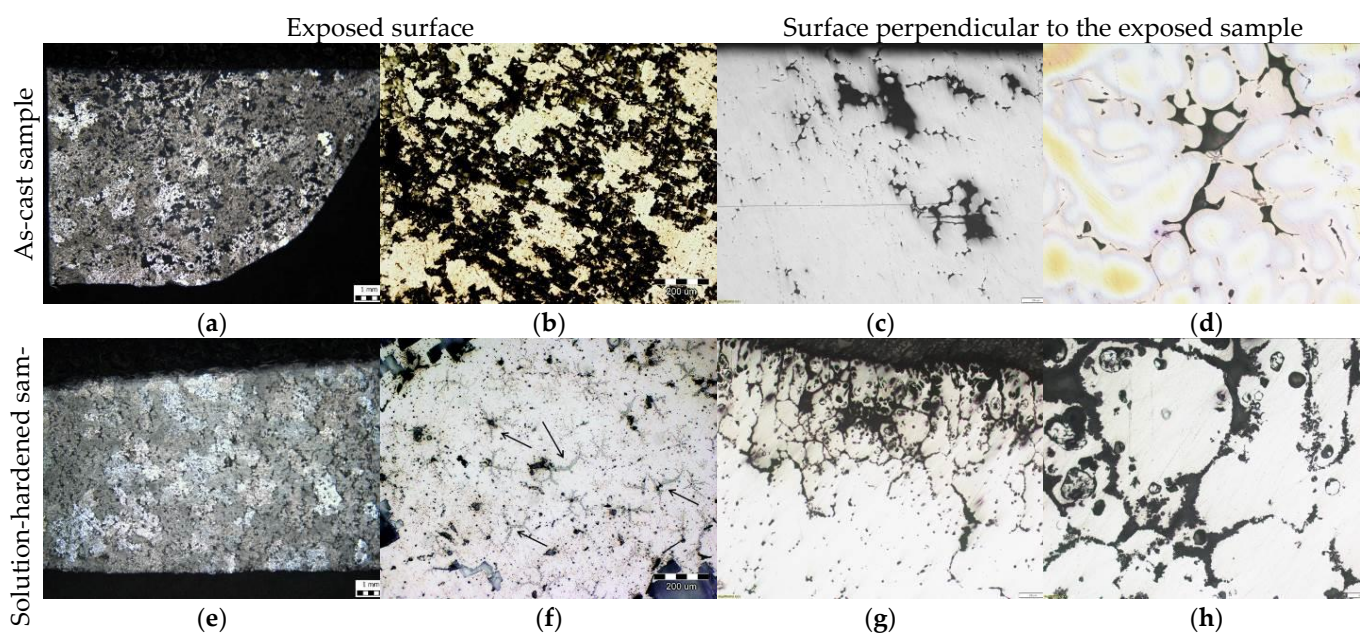


**Figure 9.** The structure of the samples after electrochemical testing: (a) macrostructure of the exposed surface of the as-cast sample; (b) microstructure of the exposed surface of the as-cast sample; (c) microstructure of the perpendicular surface of the as-cast sample; (d) phase involvement; (e) macrostructure of the exposed surface of the solution-hardened sample; (f) microstructure of the exposed surface of the solution-hardened sample; (g) microstructure of the perpendicular surface of the solution-hardened sample; (h) phase involvement and dissolution of the  $\alpha_{\text{Al}}$  matrix.

The macrostructure of the sample in as-cast condition after electrochemical testing indicates cavity formation (Figure 9a). The cavities are equally distributed across the exposed surface of the sample (Figure 9b). On the other hand, the pitting corrosion of the solution-hardened sample initiates and propagates at the grain boundaries (Figure 9e) surrounded by the precipitates (Figure 9f).

The microstructural analysis indicates cavity formation at the surface of both samples (Figure 9c,g). In the as-cast sample, the degradation progresses by the dissolution of the  $\beta$  and T precipitates located between the branches of the  $\alpha_{\text{Al}}$  dendritic network (Figure 9c,d). In the solution-hardened sample, degradation is manifested as intergranular and transgranular involving the grain boundaries and  $\alpha_{\text{Al}}$  grains. The existence of the  $\delta$  phase precipitates inside the  $\alpha_{\text{Al}}$  grains resulted in the cavity formation (Figure 9g,h).

#### 4. Discussion

The use of an induction melting furnace and a protective atmosphere of Ar enabled the synthesis of Al-2.18Mg-1.92Li. The alloy was cast into a permanent steel mold without a protective atmosphere.

The Mg content of 2.18 wt.% and lower Li/Mg ratio (Li/Mg = 0.88) implied preferred solidification of the T phase. However, the use of Thermo-Calc software support indicated

more complex microstructure development during solidification. The equilibrium solidification calculations indicated the transformation of the  $\alpha_{Al}$  dendritic network followed by solid-state precipitation of the  $\delta$ , T and  $\beta$  phases. The  $\delta$  phase precipitated from the  $\alpha_{Al}$  matrix containing 16.79 wt.% Li at 360 °C. The reduction of Li content in the  $\alpha_{Al}$  matrix to 11.46 wt.% and an increase in Mg content to 17.02 wt.% caused precipitation of the T phase at 290 °C. The equilibrium solidification ended at 89.15 °C with precipitation of the  $\beta$  phase from the Mg enriched  $\alpha_{Al}$  matrix containing 44.73 wt.% Mg. The non-equilibrium solidification sequence comprehended the transformation of the  $\alpha_{Al}$  dendritic network followed by the solidification of  $\delta$  and T phases at higher temperatures with respect to the equilibrium solidification sequence.

The results of the Thermo–Calc calculations indicated precipitation of the phases that are anodic with respect to the  $\alpha_{Al}$  matrix and located in the interdendritic regions. Based on the nature of the precipitates and their location, the Al-2.18Mg-1.92Li alloy shows a tendency towards intergranular degradation. To increase the Al-2.18Mg-1.92Li alloy microstructure stability in the corrosive environment, solution hardening was used. By dissolving all the precipitated phases and enriching the  $\alpha_{Al}$  matrix with Mg and Li, higher microstructure stability was expected. Although solution hardened led to the homogenization in grain morphology, the microstructure analysis indicated the presence of the  $\delta$  phase located inside the  $\alpha_{Al}$  grains.

The applied methods of electrochemical measurements recorded negative corrosion potential indicating the instability of both samples and their dissolution during testing. The Time dependence of open circuit potential measurements for the sample in the as-cast condition revealed less negative corrosion potential and higher resistance to microstructure degradation. The Tafel polarization curves indicated higher corrosion potential, current density, anode slope, cathode slope, and corrosion rate for the solution-hardened sample. The higher current density and anode slope are consequences of the  $\alpha_{Al}$  matrix dissolution. The higher cathode slope is attributed to the testing solution reduction and local increase in pH value. The local increase in the pH value of the testing solution led to the spontaneous passivation of the sample.

The macrostructural analysis of the exposed surface of both samples indicates cavity formation. The cavity formation is enabled by surface passive film dissolution due to the high acidity of the testing solution (0.4 pH). In the as-cast sample, the degradation progressed by the dissolution of the  $\beta$  and T phase precipitates located between the branches of the  $\alpha_{Al}$  dendritic network. In the solution-hardened sample, degradation is manifested as intergranular involving the grain boundaries and the  $\alpha_{Al}$  grains. The cavity formation in the  $\alpha_{Al}$  grains is caused by the  $\delta$  phase precipitates.

## 5. Conclusions

The research was performed to determine the microstructure degradation of the Al-2.18Mg-1.92Li alloy in as-cast and solution-hardened conditions during electrochemical testing. The alloy was synthesized to obtain improved engineering properties based on microstructure development. The improved mechanical properties and corrosion resistance are imperative for application in the transportation industry.

However, the sample in as-cast condition has lower corrosion potential (−749.84 mV) compared to the solution-hardened sample (−752.52 mV) resulting in a lower corrosion rate (17.01 mm/year). The higher corrosion rate of the solution-hardened sample (51.24 mm/year) is a consequence of the  $\delta$  phase precipitation at the grain boundaries and inside the grain of  $\alpha_{Al}$ , leading to the intergranular corrosion and cavity formation. Although the solution hardening was performed with the intention to dissolve all the precipitates and enrich  $\alpha_{Al}$  solid solution with Mg and Li, the precipitated  $\delta$  phase was not affected. The stability of the  $\delta$  phase at the temperature of 520 °C was assured by the wide solidification range.

**Author Contributions:** Conceptualization, F.K. and Z.Z.B.; methodology, F.K. and Z.Z.B.; software, S.B.; validation, F.K., S.B., Z.Z.B., and M.P.; formal analysis, F.K. and M.P.; investigation, F.K. and S.B.; resources, M.P.; writing—original draft preparation, Z.Z.B. and F.K.; writing—review and editing, Z.Z.B. and F.K.; visualization, F.K. and Z.Z.B.; supervision, Z.Z.B.; project administration, Z.Z.B.; funding acquisition, Z.Z.B. All authors have read and agreed to the published version of the manuscript.

**Funding:** This research received no external funding. The materials and laboratory equipment have been provided by collaborative companies and the Faculty of Metallurgy within research project IP-124 University of Zagreb Faculty of Metallurgy, Centre for Foundry Technology—SIMET, KK.01.1.1.02.0020 and VIRTULAB—Integrated laboratory for primary and secondary raw materials, KK.01.1.1.02.0022.

**Institutional Review Board Statement:** Not applicable.

**Informed Consent Statement:** Not applicable.

**Data Availability Statement:** Data is contained within the article. The data presented in this study can be seen in the content above.

**Acknowledgments:** The investigation was performed within the research topic “Design and Characterization of Innovative Engineering Alloys,” Code: FPI-124- 2019-ZZB funded by the University of Zagreb within the Framework of Financial Support of Research, a scientific research project within Croatian–Slovenian collaboration “Design and Characterization of Innovative Aluminum–Magnesium–Lithium alloy (2018–2019) funded by Ministry of Science and Education and Infrastructural scientific projects: Center for Foundry Technology, Code: KK.01.1.1.02.0020 and VIRTULAB—Integrated Laboratory for Primary and Secondary Raw Materials, Code: KK.01.1.1.02.0022 funded by the European Regional Development Fund, Operational Programme Competitiveness and Cohesion 2014–2020.

**Conflicts of Interest:** The authors declare no conflict of interest.

## References

1. Chen, X.; Zhao, G.; Liu, G.; Sun, L.; Chen, L.; Zhang, C. Microstructure evolution and mechanical properties of 2196 Al–Li alloy in hot extrusion process. *J. Mater. Process. Technol.* **2020**, *257*, 116348. [[CrossRef](#)]
2. Gloria, A.; Montanari, R.; Ricchetta, M.; Varone, A. Alloys for Aeronautic Applications: State of the Art and Perspectives. *Metals* **2019**, *9*, 662. [[CrossRef](#)]
3. Roy, S.; Dutta, A.; Chakraborti, N. A novel method of determining interatomic potential for Al and Al–Li alloys and studying strength of Al–Al<sub>3</sub>Li interphase using evolutionary algorithms. *Comput. Mater. Sci.* **2021**, *190*, 110258. [[CrossRef](#)]
4. Stanić, D.; Zovko Brodarac, Z.; Li, L. Influence of Copper Addition in AlSi7MgCu Alloy on Microstructure Development and Tensile Strength Improvement. *Metals* **2020**, *10*, 1623. [[CrossRef](#)]
5. Zovko Brodarac, Z.; Holjevac Grgurić, T.; Burja, J. Thermodynamic stability of AlSi11 alloy microconstituents. *J. Therm. Anal. Calorim.* **2017**, *53*, 429–439. [[CrossRef](#)]
6. Zovko Brodarac, Z.; Unkić, F.; Medved, J.; Mrvar, P. Determination of solidification sequence of the AlMg9 alloy. *Kov. Mater.* **2012**, *50*, 59–67. [[CrossRef](#)]
7. Buljeta, I.; Beroš, A.; Zovko Brodarac, Z. The Study Conditions Occurrence of Hot Tearing in the Billets Alloy EN AW6060 Produced with the Process of Direct Chill Casting. In *Light Metals 2016*, 1st ed.; Williams, E., Ed.; John Wiley & Sons, Inc.: Hoboken, NJ, USA, 2016; pp. 673–678.
8. Medjahed, A.; Henniche, A.; Derradji, M.; Yu, T.; Wang, Y.; Wu, R.; Hou, L.; Zhanga, J.; Lia, X.; Zhang, M. Effects of Cu/Mg ratio on the microstructure, mechanical and corrosion properties of Al–Li–Cu–Mg–X alloys. *Mater. Sci. Eng. A* **2018**, *718*, 241–249. [[CrossRef](#)]
9. Stanić, D.; Zovko Brodarac, Z. Influence of cooling rate on microstructure development of AlSi9MgMn alloy. *J. Min. Metall. Sect. B–Metall.* **2020**, *56*, 405–413. [[CrossRef](#)]
10. Zovko Brodarac, Z.; Mrvar, P.; Medved, J. Temperature interval determination for the performing local squeezing casting process on the AlSi10Mg alloy castings. *Kov. Mater.* **2009**, *47*, 209–2014.
11. Duan, X.; Jiang, H.; Mi, Z.; Cheng, L.; Wang, J. Reduce the Planar Anisotropy of AA6016 Aluminum Sheets by Texture and Microstructure Control. *Crystals* **2020**, *10*, 1027. [[CrossRef](#)]
12. Kozina, F.; Zovko Brodarac, Z.; Petrič, M.; Penko, A. The influence of iron impurities on the compression behavior of Al–2.24Mg–2.09Li alloy. *J. Min. Metall. Sect. B–Metall.* **2020**, *56*, 425–433. [[CrossRef](#)]
13. Hung, F.S. Design of lightweight aluminum alloy building materials for corrosion and wear resistance. *Emerg. Mater. Res.* **2020**, *9*, 750–757. [[CrossRef](#)]
14. Liu, J.; Zhao, K.; Yu, M.; Li, S. Effect of surface abrasion on pitting corrosion of Al–Li alloy. *Corros. Sci.* **2018**, *138*, 75–84. [[CrossRef](#)]

15. Guérinab, M.; Alexisb, J.; Andrieua, E.; Laffonta, L.; Lefebvrec, W.; Odemera, G.; Blanca, C. Identification of the metallurgical parameters explaining the corrosion susceptibility in a 2050 aluminium alloy. *Corros. Sci.* **2016**, *102*, 291–300. [[CrossRef](#)]
16. Darband, G.D.; Aliofkhaezaei, M.; Khorsand, S.; Sokhanvar, S.; Kaboli, A. Science and Engineering of Superhydrophobic Surfaces: Review of Corrosion Resistance, Chemical and Mechanical Stability. *Arab. J. Chem.* **2020**, *13*, 1763–1802. [[CrossRef](#)]
17. Donatusa, U.; Teradabc, M.; Ramirez, C.; Fernanda, O.; Queiroza, M.; Fatima, A.; Bugarina, S.; Costa, I. On the AA2198-T851 alloy microstructure and its correlation with localized corrosion behavior. *Corros. Sci.* **2018**, *131*, 300–309. [[CrossRef](#)]
18. Zhou, X.; Luo, C.; Ma, Y.; Hashimoto, T.; Thompson, G.E.; Hughes, A.E.; Skeldon, P. Grain-stored energy and the propagation of intergranular corrosion in AA2xxx aluminium alloys. *Surf. Inter. Anal.* **2013**, *13*, 1543–1547. [[CrossRef](#)]
19. Weiss, D. Improved High-Temperature Aluminum Alloys Containing Cerium. *J. Mater. Eng. Perform.* **2019**, *28*, 1903–1908. [[CrossRef](#)]
20. Liuab, D.; Sangb, F.; Lib, J.; Birbilisc, N.; Wangd, Z.; Mae, Y.; Zhang, Y. The role of grain structure characteristics on the localized corrosion feature in the 1445 Al-Cu-Li alloy. *Mater. Charact.* **2019**, *158*, 109981.
21. Deschamps, A.; Sigli, C.; Moureya, D.; Geusera, F.; Lefebvrec, W.; Davo, B. Experimental and modelling assessment of precipitation kinetics in an Al-Li-Mg alloy. *Acta Mater.* **2012**, *60*, 1917–1928. [[CrossRef](#)]
22. Mogucheva, A.; Kaibyshev, R. Microstructure and Mechanical Properties of an Al-Li-Mg-Sc-Zr Alloy Subjected to ECAP. *Metals* **2016**, *6*, 254. [[CrossRef](#)]
23. Wright, E.; Kaufman, M.J.; Weber, G.R. The Influence of Macrostrain Evolution by Tensile Straining on Localized Corrosion of Al-Li Alloys 2099 and 2196. *Metall. Mater. Trans. A* **2020**, *51*, 1012–1021. [[CrossRef](#)]
24. Sekhar, A.P.; Mandal, A.B.; Das, D. Mechanical properties and corrosion behavior of artificially aged Al-Mg-Si alloy. *J. Mater. Res. Technol.* **2019**, *9*, 1005–1024. [[CrossRef](#)]
25. Lunder, O.; Lein, J.E.; Aune, T.K.; Nisancioglu, K. The role of Mg<sub>17</sub>Al<sub>12</sub> phase in the corrosion of Mg alloy AZ91. *Corrosion* **1989**, *45*, 741–748. [[CrossRef](#)]
26. Kozina, F.; Zovko Brodarac, Z.; Mrvar, P.; Petrič, M. Solidification sequence of Al-2, 5wt.%Mg-0, 7wt.%Li alloy. In Proceedings of the 49th International October Conference on Mining And Metallurgy Proceedings, Bor, Serbia, 18–21 October 2017; Štrbac, N., Marković, I., Balanović, L.J., Eds.; University of Belgrade, Technical Faculty in Bor: Belgrade, Serbia, 2017; pp. 556–559.
27. Brahami, A.; Fajoui, J.; Bouchouicha, B. Numerical simulation on the effect of friction stir welding parameters on the peak temperature, von Mises stress, and residual stresses of 6061-T6 aluminum alloy. *J. Fail. Anal. Prev.* **2020**, *20*, 197–207. [[CrossRef](#)]
28. Rocheta, C.; Veron, M.; Rauch, R.F.; Lowed, T.C.; Arfaeie, B.; Laurinob, A.; Harouard, J.P.; Blanca, C. Influence of equal-channel angular pressing on the microstructure and corrosion behaviour of a 6xxx aluminium alloy for automotive conductors. *Corros. Sci.* **2020**, *166*, 108453. [[CrossRef](#)]